The following publication Li, M., Yang, H., Wang, Y., Wang, L., & Chu, P. K. (2018). Core-shell CoMoO4@Ni(OH)2 on ordered macro-porous electrode plate for high-performance supercapacitor. Electrochimica Acta, 283, 538-547 is available at https://doi.org/10.1016/j.electacta.2018.06.043.

Core-shell $CoMoO_4@Ni(OH)_2$ on Ordered Micro-Porous Electrode Plate as the composite structured electrode for high performance supercapacitor

Mai Li[a*], Hongxing Yang[a*], Yuanhao Wang[b], Lianwei Wang[c] and Paul K Chu[d]

a Renewable Energy Research Group, Department of Building Services Engineering, The Hong Kong Polytechnic University, Hung Hom, Kowloon, Hong Kong, China
b Faculty of Science and Technology, Technological and Higher Education Institute of Hong Kong, New Territories, Hong Kong, China
c Key Laboratory of Polar Materials and Devices, Ministry of Education, Department of Electronic Engineering, East China Normal University, 500 Dongchuan Road, Shanghai 200241, P. R. China
d Department of Physics and Material Science, City University of Hong Kong, Tat Chee Avenue, Kowloon, Hong Kong, China
* Corresponding author: Tel.: +852 56065568; Fax: +852 2766 7198.
E-mail address: mai.li@polyu.edu.hk.

Abstract

Multidimensional core–shell $CoMoO_4@Ni(OH)_2$ nanocomposite materials are fabricated on the surface and side wall of an ordered macro-porous electrode plate (OMEP) by a multi-step hydrothermal process as the active electrode in a high power density storage device. The effects, morphology, forming mechanism of the $CoMoO_4@Ni(OH)_2$ composite materials, as well as capacitor features, are systematically investigated in this paper. Compared with the nanostructured nickel growth on the OMEP or the $CoMoO_4@Ni(OH)_2$ on nickel covered silicon wafer with the same area, the as-prepared $CoMoO_4@Ni(OH)_2$/OMEP has shown an enhanced electrochemical energy storage properties, manifesting a high energy capacitance of 8.55 F g^{-1} (1858.70 F cm^{-2}) at 2 mA cm^{-2} and good cycling stability of 99.6% capacity retention after 5,000 cycles. The asymmetrical supercapacitor (ASC) device was assembled using a polyethylene (PE) membrane, the $CoMoO_4@Ni(OH)_2$/OMEP and active carbon covered nickel foam. The PE membrane as a separator was first ultrasonic cleaned, soaked in KOH for 5 min and then assembled into three parts in a standard

RS2032 battery shell using the quasi solid electrolyte. The ASC fabricated by the $CoMoO_4@Ni(OH)_2$/OMEP has an energy density of 9.66 Wh Kg^{-1} even at the power density of 3,000 W Kg^{-1}, which is comparable to the results from relative researches. The sealed ASC also exhibits stable power characteristics (10,000 cycles with 86.5% retention at a current of 0.06 A). The device produces large instantaneous power to be charged in 10 s and one ASC can power a 5mm red LED with high efficiency.

Keywords: Supercapacitors; Ordered through Micro-Porous Electrode Plate; Energy storage; core-shell nanocompound; Hybrid device.

1. Introduction

With the technological and scientific advancements in the 21st century, our modern society requires higher charging-discharging efficiency, larger energy density and longer lifespan energy storage devices. For this purpose, supercapacitors have been used in many applications, such as power back-up, pacemakers, electrical vehicles and air bags to complementary those of rechargeable devices such as batteries and fuel cells to improve the overall performance of the devices[1, 2]. More attention has been focused on the new ways to fabricate the high performance supercapacitors that can store a large amount of energy and provide a more power within a very short time. According to the charge storage mechanisms and properties of active materials, super capacitors can be divided into two types of electric double layer capacitors (capacitor) and pseudocapacitors (PCs) [3]. In particular, PCs based on ion adsorption and desorption like electric double-layer charge (EDLC) on the electrode surface as well as the fast reversible faradic redox reactions usually provide larger specific capacitance than the supercapacitors composed of carbonaceous materials based mainly on the EDLC storage [4, 5]. Therefore, more researches have focused on the PCs due to the specific capacitance of some hydroxide-based pseudocapacitive materials, transition metal oxides or the combination of them such as MnO_2[6, 7], V_2O_5[8], Fe_2O_3[9]， Co_3O_4[10, 11]， CoO[10, 12] and NiO[13, 14] because of their low cost, easy to mass production and great structures and morphology flexibility.

Among these transition metal oxides, $Ni(OH)_2$ has attracted more attention due to its environmentally friendly nature, low cost, and possesses enhanced electrochemical properties resulting from high electrochemical activity and good electrical conductivity [15]. As the research given by Zhou et al [16], $Ni(OH)_2$ nanosheets coated onto single-crystal Ni_3S_2 nanorods grown on the surface of the three-dimensional graphene network (3DGN), demonstrating specific capacitance of 1037.5 F g^{-1} at a charge and discharge current density of 5.1 A g^{-1}. However, the structured $Ni(OH)_2$ nanosheets generally suffer from weak cycling ability or rate performance due to its limited kinetics during the redox reaction and agglomeration caused by nanoscale effects that limiting its practical application [17-19]. To alleviate those issues, our study inherited and developed the existing research, and the $Ni(OH)_2$ nanosheets was grown uniform on the surface and sidewall of $CoMoO_4$ covered ordered Macro-Porous Electrode Plate (OMEP) as both conductive substrate and the active electrode for multi-dimensional macro/nano composite structured electrode that having stable supporting structure to prevent the agglomeration of $CoMoO_4$@$Ni(OH)_2$. Meanwhile, the uniform and stable nickel layer coating on OMEP greatly promote the conductivity of the electrode, so that the high energy density and stability of the nanoscale structured electrode improved tremendous. Fig. 1 vividly reveals the advantages of the large specific surface area design concept of OMEP that improve the performance of the device by optimizing the electrode structure. Based on the characterization of the coating structure and the multi-dimensional nanostructure, the influence mechanism of the interfacial characteristics on the growth of the composite nanocrystals is discussed that provide a theoretical support for the development of multidimensional supercapacitor electrode materials.

So far, the main synthesis strategies of the active materials of the electrode are including hydro-solvothermal routes,[20] liquid-phase co-precipitation,[21] electrodeposition methods,[22] microwave-assisted methods,[23] high-temperature synthesis [24] and electrospinning methods[25]. Actually, analysis from the formation mechanism of the nanomaterials, we can find that conventional methods of synthesis nanomaterials under normal temperature and pressure is difficult to deposit a large amounts of nanomaterials uniformly in the interior of the high aspect ratio macro-porous structure. Therefore, among those methods, as a comparison, the hydrothermal synthesis route has several advantages for nanomaterials growth in the surface and inter wall of OMEP. First of all, synthesis and growth of nanomaterials in a stable environment, the active substances can be grown directly on the surface and internal of the OMEP and so the microstructure of the $CoMoO_4$@$Ni(OH)_2$ nanostructure could be preserved. Secondly, the active substances can be grown on the surface of nanoscale nickel as nucleation center on OMEP directly without adding conduction agent or polymer binder, and so the fabricated electrode can directly reflect the performance characteristics of the specific active substances. Thirdly, since the chemical reaction conduct under high pressure and temperature that the reaction solution can be easily flowed into the macroporous of the OMEP, so that the $CoMoO_4@Ni(OH)_2$ nanosheets could uniform grown on the surface and inter channel of OMEP[26].

Two step method was used to deposit nano-scale Ni onto the surface and channel of Si-MCPs as shown in FigS1, and the nickel with roughly morphology on the Si-MCPs can serve as nucleation centers for nanomaterials as well as excellent electrical conductive layer for the electrode. $CoMoO_4@Ni(OH)_2$ is deposited to the radically ordered OMEP to form the $CoMoO_4@Ni(OH)_2$/OMEP core-shell nanostructure by hydrothermal self-assembly with different reaction conditions and then a serious experiments carried out based on those samples. Moreover, the asymmetric pseudocapacitor (ASC) [27] was also fabricated with the structure of $CoMoO_4@Ni(OH)_2$/OMEP as the positive electrode and activated carbon mixed with acetylene black as the negative electrode and investigate in this research.

2. Experimental details

2.1 Chemicals

The reagents including sodium hypophosphite monohydrate [$NaH_2PO_2 \cdot H_2O$], nickel chloride [$NiCl_2 \cdot 6H_2O$], nickel nitrate [$Ni(NO_3)_2 \cdot 6H_2O$], ammonium chloride [NH_4Cl], ammonium [$NH_3 \cdot H_2O$], cobalt nitrate [$Co(NO_3)_2 \cdot 6H_2O$], ammonium molybdate tetrahydrate [$(NH_4)_6Mo_7O_{24} \cdot 4H_2O$], ammonium fluoride [$NH_4F$] and urea [$CO(NH_2)_2$]. All of the chemical reagents are AnalaR grade. 18 MU de-ionized water were used to prepare the aqueous solutions and all the series samples were fabricated at room temperature.

2.2 Fabrication of the perforation nano Ni covered Ordered Macro-Porous Electrode Plate (OMEP)

The Ni layer was deposited on both surface and inter channel of the silicon macrochannels (Si-MCPs) as illustrated in Fig. S1(a). The chemical deposition as the first step to fabrication the OMEP was based on Si-MCP and the Si-MCPs used here was fabricated through liquid flow deposition method according to Wang et al[28]. To further improve the conductivity and surface area of the OMEP, porous nano nickel shown in Fig. S1(b)-(d) was also manufactured by the electro-chemical nickel plating method given by Li et al[26]. After completing the production of perforation low resistance nano Ni covered OMEP, further experiments were carried out based on it.

2.3 Synthesis of 3-Dimensional $CoMoO_4@Ni(OH)_2/OMEP$ electrode

$CoMoO_4$ was prepared hydrothermally. The Ordered Macro-Porous Electrode Plate (OMEP) was cut into pieces with a size of 0.7*0.8 cm, and in order to improve the hydrophilicity of the OMEP, it was placed into Triton X-100 as the buffer solution for at least 10 minutes, and then put the cutting OMEP into a Teflon-lined autoclave. The reaction chemical solution was prepared by blending 2 mmol of $Co(NO_3)_2 \cdot 6H_2O$ and 2 mmol of $(NH_4)_6Mo_7O_{24} \cdot 4H_2O$ in 100 mL through 18 MΩ de-ionized water with ultrasonic stirring, after that transferred the solution into the Teflon-lined stainless steel autoclave liner. The reaction proceeded for 2.5 h at a temperature of 120 ℃, resulting in the formation of a violet precipitate on the surface.

$Ni(OH)_2$ was prepared by a hydrothermal method. The cleaned $CoMoO_4/OMEP$ was placed standing against the wall of a 40 ml Teflon-lined stainless steel autoclave. The reaction solution was obtained by mixing 2 mmol $Ni(NO_3)_2 \cdot 6H_2O$, 10 mmol NH_4F, and 10 mmol urea in 40 mL of distilled water under magnetic stirring and transferred the solution into the Teflon-lined autoclave liner. After reacting for 12 h at 160℃, the OMEP with the as-grown hydrate precursors was dried at 80℃ for 2 h and annealed at 300℃ for 2 h in Ar to obtain the $CoMoO_4@Ni(OH)_2/OMEP$. In order to study the composite materials growth on the plane structure, $CoMoO_4@Ni(OH)_2$ was prepared on a Nickel plate (NP) for comparison. The fabrication steps and size of $CoMoO_4@Ni(OH)_2/NP$ was the same as those of $CoMoO_4@Ni(OH)_2/OMEP$.

2.4 Characterization and Fabrication of Asymmetrical Device

The microstructure and morphology of the OMEP and $CoMoO_4@Ni(OH)_2$ thin films were determined by X-ray diffraction (XRD, Rigaku, RINT2000, Japan) and scanning electron microscopy (FE-SEM, JEOL JSM-7001F, Japan). Elemental composition was determined by the X-ray photoelectron spectroscopy (XPS, Kratos AXIS Ultra DLD). The TEM image, SAED, lattice structure and EDS mapping was determined by transmission electron microscopy (STEM, Jeol JEM-2100F). Three-electrode Shanghai Chenhua CHI660D electrochemical working station were used to estimate the electrochemical behavior of the electrodes in 2 M KOH aqueous at the room temperature. Furthermore, the specific capacity and electrochemical properties of the electrode samples were carried out by CV scans (vs. SCE) at various scanning rates conducted in a potential range between -0.2-0.6V and chronopotentiometry tests conducted in a potential range between 0-0.4V at various constant current densities, respectively. The measurements of ASC were carried out to estimate the commercial value of the composite materials according to the CV scans from 0 to 1.5 V, charging-discharging tests from 0 to 1.5 V, as well as real application tests. Impedance spectra were acquired from $CoMoO_4@Ni(OH)_2$/OMEP and ASC before and after the cycling test from 0.01 to 10,000 Hz to investigate the reaction mechanism of the electrode and device.

The asymmetrical supercapacitor (ASC) device was assembled using a polyethylene (PE) membrane, the $CoMoO_4@Ni(OH)_2$/OMEP and active carbon covered nickel foam. The PE membrane as a separator was first ultrasonic cleaned, soaked in KOH for 5 min and then assembled into three parts in a standard RS2032 battery shell using the quasi solid electrolyte. The specific capacitance (C_m), area capacitance(C_a), energy density (E in Wh kg^{-1}) and power density (P in W kg^{-1}) of the electrodes and asymmetrical device were calculated according to the following formulas:[29]

$$C_m = \frac{I \times \Delta t}{m \times \Delta V} \quad (1)$$

$$C_a = \frac{I \times \Delta t}{\mathrm{S} \times \Delta V} \quad (2)$$

$$E = \frac{1}{2} C(\Delta V)^2 \quad (3)$$

$$P = \frac{E}{\Delta t} \quad (4)$$

where C (F g^{-1}) is the specific capacitance and C (F cm^{-2}) is the area capacitance of the electrode according to the m (g) mass of the active materials and S (cm^2) effective area of the working electrode, respectively, I (A) is the current of the electrode discharging process, Δt (s) is the discharging time and (V) is the potential difference value.

3. Results and discussions

After fabrication of the OMEP with a rough morphology and excellent electrical conductivity[30], a two-step hydrothermal method is employed to synthesize the active materials at a high temperature and pressure, so that the solution can easily penetrate the nanoscale electrode substrate and the core-shell $CoMoO_4@Ni(OH)_2$ composite structure is prepared uniformly on the surface and sidewall of the 3D OMEP as shown in Fig.4. The thin $Ni(OH)_2$ and $CoMoO_4$ films are also deposited on the OMEP and $Ni(OH)_2@CoMoO_4$ on nickel plate (NP) by hydrothermal for comparison and the electrochemical properties and effects of the solvents on the morphology of those samples are determined from an active area of 0.5 cm^2. Moreover, the asymmetric pseudocapacitor (ASC) is prepared through supercapacitor making process to estimate the practical value of the $Ni(OH)_2@CoMoO_4$ composite materials.

3.1 Materials Characterization

XPS survey spectrum and the valence states of nickel, cobalt and oxygen in $CoMoO_4@Ni(OH)_2$/OMEP are determined by XPS. As shown in the survey spectrum of Fig. 2(a), the presence of Ni, C, O, Co and Si are consistent with XRD [Fig. 5(a)] and EDS [Fig.S2]. The Ni 2p spectra presented in Fig. 2(b) is fitted using the XPSPEAK41 software, and it shows two major peaks located at around 855.7 eV and 873.4 eV with a spin-energy separation of 17.7 eV. These results are in accordance with the data of Ni $2p_{3/2}$ and Ni $2p_{1/2}$ which are the characteristics of the $Ni(OH)_2$ phases [31]. As shown in Fig. 2(c), the binding energies of the Co $2p_{3/2}$ and Co $2p_{1/2}$ photoelectrons are 779.8, 780.3, and 781.1 eV corresponding to Co_3O_4, CoOOH and $CoMoO_4$, respectively [32, 33]. The Mo 3d core-level spin–orbit doublets (at 232 and 235 eV) in Fig. 3(e) are in accordance with the reported value of a splitting width of 3.0 eV [34, 35]. The Mo^{6+} peak is attributed to surface Mo species that have been oxidized upon air exposure.

In this work, we report an innovative strategy to fabricate nanocomposite $CoMoO_4$@$Ni(OH)_2$ films via hydrothermal synthesis route based on nano Ni covered Ordered Micro-Porous Electrode Plate (OMEP) with a large aspect ratio for the production of new type supercapacitors. The OMEP with millions of inner channels provide the necessary space for the nickel conductive layer and the $CoMoO_4$@$Ni(OH)_2$ active material in the supercapacitors. The surface morphology of the nanoscale $CoMoO_4$/OMEP is shown in Fig.3 and the $CoMoO_4$@$Ni(OH)_2$/OMEP is shown in Fig4. The advantage of the large surface area for the $CoMoO_4$@$Ni(OH)_2$ nanosheets is maintained, at the same time the overall footprint of the whole electrode can be reduced obviously due to the nanosheets on the sidewall of the OMEP.

Fig.3. (a)-(c) show the morphological features of the cobalt molybdate nanostructure on the surface of OMEP as observed by SEM at different magnifications. After hydrothermal synthesis, according to Fig. 3(b) and (c) of the higher magnification SEM images, a compact $CoMoO_4$ nanoflower about 300 nm thick and 2 μm length is formed with the interconnected multi-level structure network on the surface of OMEP. Fig. 3(d)-(f) exhibit the SEM images of the $CoMoO_4$ nanopillars from the inner side wall of the OMEP with different magnifications. An even nanopillars surface have a typical length around 2 μm and width of less than 200 nm grow inside the pores. The

Ni particles on the OMEP provide a vast quantity of nucleation center for growth of the $CoMoO_4$ nanopillars thereby resulting in a strong bonding of the nanopillars with the OMEP. As shown in Fig. 4(a) and (b), the $Ni(OH)_2$ nanosheets grown on OMEP have an ultrathin structure with a typical thickness of 5 nm and so they can easily spread and growth on the surface of other nanomaterials. Fig. 4(c) and (d) shows that the $CoMoO_4$@$Ni(OH)_2$ on the surface of the OMEP increases the area and amount of active materials per unit area. Fig. 4(f) display the enlarged SEM image of a local area in Fig. 4(e) revealing ultrathin $Ni(OH)_2$ nanosheets grown on the surface of CoMoO4 nanopillars that formed a special core-shell structure. The morphology of the $CoMoO_4$@$Ni(OH)_2$ in the channel has a similar structure to that growth on the surface of $CoMoO_4$/OMEP, which promote transport of electrons, space utilization and contact area of the active materials with the electrolyte. The nano materials in the surface and the sidewall of the OMEP work together to improve the contact area of nanomaterials active material with the electrolyte that leading to high area capacity.

X-ray diffraction (XRD) is conducted to determine the phase structure of the electrode. The backbone material OMEP (Ni: JCPDS card no. 01-089-7128) is identified by the XRD pattern from the Fig. 5(a) (bottom black line) and the hierarchical $CoMoO_4$ nanostructure under violet line (α-$CoMoO_4$: JCPDS card no. 00-021-0868) and $Ni(OH)_2$ (α-$Ni(OH)_2$: JCPDS card no. 22-0444) under green line and $CoMoO_4$@$Ni(OH)_2$/OMEP are also shown in Fig. 5(a) respectively [33, 36]. The structure of the as-synthesized $CoMoO_4$@$Ni(OH)_2$ composite material was further investigate by the transmission electron microscopy (TEM). TEM image of $CoMoO_4$@$Ni(OH)_2$ is shown in the Fig.5(b) and (c) and the selected-area electron diffraction (SAED) pattern of the representative nanocomposite is shown in the inset of Fig. 5(b). The HR-TEM image in Fig. 5(d) reveals a 0.277 nm lattice fringes in the background of the composite material, corresponding to the (-131) plane of α-$CoMoO_4$ and a 0.46 nm lattice fringes in the surface materials corresponding to the (001) plane of α-$Ni(OH)_2$. The elemental composition of $CoMoO_4$@$Ni(OH)_2$/OMEP is also determined by EDS and the elemental maps of Fig. S2 indicate uniform distributions of nickel, cobalt, molybdenum and oxygen on the particles.

In order to further confirm that the successful of the combination the two substances of α-$CoMoO_4$ and α-$Ni(OH)_2$ together and specific crystal orientation in the process of material growth, the lattice structure of those materials have been simulated of by software as shown in Fig5(f). According to the fitting result, the distance among (-131) plane (Fig.S3(a)) of α-$CoMoO_4$ (base-centered monoclinic space group C2/m, ICSD # 23808) is 0.277nm and the distance among (001) plane (Fig.S3(b)) of α-$Ni(OH)_2$ (base-centered trigonal/rhombohedral space group P-3/m, ICSD # 28101) is 0.463nm that fit well with the result getting from STEM [37-39]. All of the characterization from the instruments indicated that the ultra-thin nanosheet structure was successfully prepared on the surface and sidewall of OMEP.

3.2 Electrochemical Characterization

Cyclic voltammetry (CV) and chronopotentiometric (CP) methods were performed to confirm the specific (area) capacitance and electrochemical properties of the produced electrodes.

Fig. 6(a) indicated that $CoMoO_4$@$Ni(OH)_2$/OMEP reflect a much larger capacitance because of its larger enclosed area in the CV curve [Fig. 6(a), 5 mV s^{-1}] and longer discharging time [Fig. 6(b), 4 mA cm^{-2} current density] than OMEP, $CoMoO_4$@$Ni(OH)_2$/NP, $CoMoO_4$/OMPE and $Ni(OH)_2$/OMEP. Consistent with CV, chronopotentiometric at the current density of 4 mA cm^{-2}, the discharging time of OMEP (15.37s) and $CoMoO_4$/$Ni(OH)_2$ fabricated on 2D plate (57.80s) are negligible and meanwhile, $CoMoO_4$/OMPE and $Ni(OH)_2$/OMEP show a discharging time of 305.78s and 128.46s, respectively. As expected, $CoMoO_4$@$Ni(OH)_2$/OMEP shows longer discharging time of 832.86s because the nanostructured 3D OMEP has more active materials with complex composite structures with large specific surface area that promotes the activity of $CoMoO_4$@$Ni(OH)_2$ on the surface of OMEP, as shown in Fig.

6(c) and (d), compared with $CoMoO_4$@$Ni(OH)_2$/OMEP, $Ni(OH)_2$/OMEP has a clearer oxidation peak and reduction peak that may due to the closely contact of nanoscale $Ni(OH)_2$ with the OMEP increased the efficiency of ion transmission, the electron could transmitted directly to the surface of active substance. A series of CV curves acquired at various scanning rates of 5 to 200 mV s^{-1} from $CoMoO_4$@$Ni(OH)_2$/OMEP with a large enclosure are displayed in Fig. 6(e) and the peak current is increased gradually as the scanning rate improved. The square root of the scanning speed is proportional to the peak current, the reverse scanning current is almost instantaneous, which indicate that the electrode has excellent electrochemical performance and the electrode impedance is small. The reduction and oxidation peaks are obvious with similar peak shape. The probable reaction of the active materials are listed as follows:

$$3[Co(OH)_3]^- \leftrightarrow Co_3O_4 + 4H_2O + OH^- + 2e^- \quad (1)$$

$$Co_3O_4+OH^-+H_2O\leftrightarrow 3CoOOH+e^- \quad (2)$$

$$CoOOH+OH^-\leftrightarrow CoO_2+H_2O+e^- \quad (3)$$

and

$$Ni(OH)_2 + OH^- \leftrightarrow NiOOH + H_2O +e^- \quad (4)$$

The pair of visible redox peaks in the CV curves confirm well with reactions (1)-(4), suggesting that the measured electrodes are dominated by electrochemical Faraday oxidation reduction mechanisms, rather than a pure electric double layer capacitor. Even at a large scanning rate of 200 mV s^{-1}, the CV from $CoMoO_4$@$Ni(OH)_2$/OMEP shows a faster current response indicating the fast ion exchange capacity of our electrode is comparable with EDLC.

To assess the practical application of the core-shell $CoMoO_4$@$Ni(OH)_2$ nanocomposite based electrodes, the chronological potential characteristics of $CoMoO_4$@$Ni(OH)_2$/OMEP are carried out at the current densities from 2 to 32 mA cm^{-2}. From the chronopotentiometric results in Fig.6(f), the total active material load of 4.6 mg cm^{-2} and formula (1) and (2), the SC values are calculated to be 8.55, 7.31, 6.15, 4.82 and 3.83 F cm^{-2} (1858.70, 1589.13, 1336.96, 1047.83 and 832.61 F g^{-1}) for discharge current densities of 2, 4, 8, 16 and 32 mA cm^{-2}, respectively. The areal capacitances obtained from $CoMoO_4$@$Ni(OH)_2$/OMEP are much larger than those from the MoO_3/$Ni(OH)_2$ (1510 F g^{-1} at a scan rates of 1 mV s^{-1}) described by Zhu et al.[40]; Ni–Co–S/G hybrid electrodes (1492 F g^{-1} at the current density of 1 A g^{-1}) reported by Yang et al [41]; Co_3O_4@$Ni(OH)_2$ NAs (912 F g^{-1} at the current density of 1 A g^{-1}) by Zhang et al [42]; $CoMoO_4$@Co_3O_4/OMEP (1168 F g^{-1} at the current density of 0.6 A g^{-1})described by Li et al[33] and the specific capacitance is comparable to those obtained from the porous $Ni(OH)_2$ nanocubes (1842 F g^{-1} at current density of 1 A g^{-1}) prepared by Li et al [42]; g−C_3N_4@$Ni(OH)_2$ Honeycomb Nanostructure (1768.7 F g^{-1} at current density of 7 A g^{-1}) given by Dong et al [42]

The electrode of $CoMoO_4$/$Ni(OH)_2$ fabricated on the surface of nickel plate was also tested through CV and CP as well as the SEM. As shown in Fig.7(a) and (b), the capacity of $CoMoO_4$/$Ni(OH)_2$/NP is small, while the electrode has a good rate capability that indicate the material has a potential commercial value. This feature can also be seen from the Fig.S4. As the test results shown in Fig7 (d), the electrodes were subjected to long-term performance tests for evaluation of the stability of the composite structure. The $Ni(OH)_2$/OMEP shows a 41.01% sharp capacitance drop probably due to $Ni(OH)_2$ has a relatively low stability and easy to agglomeration during the cycling. The capacitances of $CoMoO_4$/OMPE, $CoMoO_4$@$Ni(OH)_2$/NP and $CoMoO_4$@$Ni(OH)_2$/OMEP are stable for 5,000 cycles with capacitance retention of 91.18%, 86.71% and 87.42% after 5,000 cycles at a current density of 50 mA cm^{-2}, respectively. While the capacitance of $CoMoO_4$@$Ni(OH)_2$/OMEP shows a relative large retention compare with pure $Ni(OH)_2$ electrode may because the $CoMoO_4$ as the very stable active substance as well as the support materials has a stable electrochemical properties with the good combination that relieving the agglomeration of $Ni(OH)_2$, at the same time improve the stability of composite nanomaterial structure that optimize the overall performance of the electrode.

EIS is performed on the $CoMoO_4$@$Ni(OH)_2$/OMEP electrodes from 0.01 Hz to 100,000 Hz with AC perturbation of 5 mV. Fig. 7(e) shows the EIS data obtained at two different stages, the newly fabricated electrode and the sample after 5,000 cycles. The equivalent circuit in the inset of Fig. 7(e) are used to fitting the impedance spectra and the fitting results are shown in Table 1.[43] For the interpretation of these fitting components can be found in the previous article, here is not to repeat.[43-46] Table 1 shows that the fabricated initial sample has an R_1 value of 2.34 Ω and after 5,000 cycles, it is 2.11 Ω indicating excellent conductivity nature of our electrode. The initial value of R_2 is 5.65 Ω, after 2,500 cycles is 1.21 Ω and after 5,000 cycles is 2.84 Ω which is consistent with the parameters of the double layer capacitor $CPE_{1\text{-}n}$ of $CoMoO_4$@$Ni(OH)_2$/OMEP (1.35), after 2,500 cycles (1.39) and after 5,000 cycles (1.24). $CoMoO_4$@$Ni(OH)_2$/OMEP after 2,500 cycling test yields a bigger double layer capacitance that may due to the complete contact of the active materials with the electrolyte. The capacitance is a pseudo one and so the parameters R_3 and $CPE_{2\text{-}n}$ are the essential indicators. R_3 values before, after 2,500 and 5,000 cycling are 26.32, 1.73 and 10.95, respectively, because most of the nanostructure is activated by the reciprocal chemical reactions and take part in the reaction. Comparison of $CPE_{2\text{-}n}$ shows that the newly made sample has a $CPE_{2\text{-}n}$ of 0.47 that is smaller than that after cycling of 1.24 [47]. Furthermore, the slope of the impedance plots at low frequencies ($CPE_{3\text{-}n}$) of the sample after 2,500 cycling is 0.87, while after 5,000 cycling is 0.76. This indicates that the intact and unobstructed of newly fabricated sample enables a quick ion diffusion through the inter channels of the OMEP while after 5,000 cycles, some of the structure collapses as shown in the Fig.7(f) of the $CoMoO_4$@$Ni(OH)_2$ on the side wall of OMEP.

3.3 Electrochemical Characteristics of the $CoMoO_4$@$Ni(OH)_2$/OMEP based ASC

To further assess the commercial potential of $CoMoO_4$@$Ni(OH)_2$, the asymmetrical supercapacitor (ASC) device was assembled using a polyethylene (PE) membrane, the $CoMoO_4$@$Ni(OH)_2$/OMEP and active carbon covered nickel foam. The PE membrane as a separator was first ultrasonic cleaned, soaked in KOH for 5 min and then assembled into three parts in a standard RS2032 battery shell using the quasi solid electrolyte. [48]. As shown in Fig. 8(b), the CV curve tends to be smooth after reaching the peak, and the angle at the turning point of the curve is approximately perpendicular to the ordinate, suggesting good electrochemical reversibility and small electrode resistant. Furthermore, even at a scan rate of 400 mV s^{-1}, the CV curve do not have obvious distortion corroborating the large comparative area and rapid ion diffusion capability of the composite nanostructures on OMEP resulting in the quick charging-discharging response of the ASC [16].

The discharging test of the ASC is carried out at various current. As shown in Fig. 8(b) of the discharge curve shows a good current platform at around 1.2V and the discharge times become shorter in certain proportions as the discharge current increases that indicate our experiments carried out in the same situation. The relationship between the specific capacitance and current density during discharging can be calculated from formula (1) which shows that the capacitance of the device is up to 210.33 at a current density of 0.25 g^{-1}. Fig. 8(c) reflects the ASC exhibits excellent cycling characteristics under a large current of 60mA, which has rarely been demonstrated from encapsulated capacitor device. After the activation process, the capacitance stabilized and has an 86.5% city retention rate in the following 10,000 cycles.

To explain the significant capacity change process of the ASC with cycling test, EIS is carried out. Nyquist plots after of newly fabricated device and the after 10000th charge-discharge cycles are exhibited in Fig. 8(d) and the corresponding equivalent circuit and the fitting parameters are also presented in Fig. 8(d). For the interpretation of these fitting components can be found in the previous article and the mechanism can be analyzed as follows [57]. According to the fitting parameters, the contact resistance R_1 of the sample after 10,000 cycles is 3.92 Ω which is larger than that of the initial sample (2.62 Ω) because the electrolyte has dried up during the long time chemical reactions that improve the contact resistance. In addition, resistance R_2 associated with the SEI layer of the newly fabricated ASC is 17.98 Ω, which is smaller than the sample after 10,000 cycles of 23.29 Ω that may due to less contact between active substance and electrolyte after the reaction under the large current density. R_3 as the diameter of the arc after test is smaller than that of the original sample. This can be attributed to the decrease of capacitance with reaction that gradually reduce OH^- diffusion from the reaction interface to the volume of OMEP[58].

The energy densities and power densities of the $CoMoO_4$@$Ni(OH)_2$/OMEP in the assembled ASC are calculated according to the formula described in (3) and (4) above and shown in Fig. 8(e) and Table 2. The mass of the active material of $CoMoO_4$@$Ni(OH)_2$ on the electrode and discharge time are used to calculate of energy densities and power densities. In addition, literature values of $CoMoO_4$ and Ni(OH)2 are given for comparison in Fig. 8(e). The ASC delivers a maximum energy density of 65.73 W h kg^{-1} at power density of 187.5 W kg^{-1} and even at 3000 W kg^{-1}, the device still shows an energy density of 9.66 W h kg^{-1}. Compared with other relevant researches, this research is better than most of related researches such as $NiCo_2S_4$@$Ni(OH)_2$//AC (53.3 W h kg^{-1} at 290 W kg^{-1})[53], PMNC/G-2//AC (41 Wh kg^{-1} at a power density of 216 W kg^{-1})[52], MnCoLDH@$Ni(OH)_2$ (47.9 W h kg^{-1} at 750.7 W kg^{-1}) and YNi-2//AC (58.4 W h kg^{-1} at 150.048 W kg^{-1})[51] and comparable to H-TiO_2@$Ni(OH)_2$//N–C (70.9 W h kg^{-1} at 102.9 W kg^{-1})[50] and $Ni(OH)_2$/MnO_2@CNT//APDC (126.4 W h kg^{-1} at 424.1 W kg^{-1})[59]. The excellent electrochemical performance of the core-shell $CoMoO_4$@$Ni(OH)_2$ nanocomposite that overcomes the problems from $Ni(OH)_2$ of the weak conductivity and weak adhesion to the nickel substrate. The cyclic performance and specific capacity of the core-shell nanomaterial have been improved. Combined with certain new base structures, such as OMEP, the material's morphology and performance characteristics are better displayed, which provides a useful platform for the research of new materials.

As shown in Fig. 8(f), the four parallel programmable LED arrays made up of 1936 small LED (11*44*4) and programmable chips compiling “Polyu” were powered by the three as-assembled ASCs in parallel after charging each device with a large current about 10 s under the voltage about 2.8V. The 5mm red LED is also powered efficiently by one as-assembled ASC that can provide a voltage of more than 1.59 V, thus illustrating that our device has good supercapacitive characteristics and provide a new reference for the application of traditional $Ni(OH)_2$ materials in the field of supercapacitor in energy storage area.

Conclusions

The mechanism, effects and electrochemical performance of the ultrathin cobaltite oxide nanosheets coated with OMEP fabricated by the hydrothermal method are investigated. The structure with the ultrathin $CoMoO_4@Ni(OH)_2$ nanosheets film reflected much higher specific capacitance than nickel covered OMEP. This can be attributed to the regular nano-structure with large specific surface area consisting of microporous and faster redox reaction of $CoMoO_4@Ni(OH)_2$ laying out by OMEP. The highest area (specific) capacitance of 8.55 F cm^{-2} (1858.70 F g^{-1}) was achieved at a current density of 50 mA cm^{-2} with an excellent electrochemical stability up to 5,000 cycles. The asymmetric supercapacitor device composed of the $CoMoO_4@Ni(OH)_2$/OMEP//AC delivers higher specific energy density at different power densities and excellent cycling stability. The ultrathin $CoMoO_4@Ni(OH)_2$ composite materials is promising and bridges the gap between traditional energy storage and power generation device.

Acknowledgements

This research was supported by the Postdoctoral Fellowships Scheme and the research funding from Research Institute for Sustainable Urban Development, The Hong Kong Polytechnic University. Support from the National Key R&D Program of China is appreciated (the Research and Demonstration of Key Technology of Net-Zero Energy Building with project number: 2016YFE0102300).

References

1. Sheberla, D.; Bachman, J. C.; Elias, J. S.; Sun, C.-J.; Shao-Horn, Y.; Dincă, M., *Nature Materials* **2016,** *16*, 220. DOI 10.1038/nmat4766 https://www.nature.com/articles/nmat4766#supplementary-information.
2. Lin, Y.; Gao, Y.; Fan, Z., *Advanced Materials* **2017,** *29* (43), 1701736-n/a. DOI 10.1002/adma.201701736.
3. Chuo, H. X.; Gao, H.; Yang, Q.; Zhang, N.; Bu, W. B.; Zhang, X. T., *Journal of Materials Chemistry A* **2014,** *2* (48), 20462-20469. DOI 10.1039/C4TA05319B.
4. Huang, H.; Lei, C.; Luo, G.; Cheng, Z.; Li, G.; Tang, S.; Du, Y., *Journal of Materials Science* **2016,** *51* (13), 6348-6356.
5. Gao, Z.; Bumgardner, C.; Song, N.; Zhang, Y.; Li, J.; Li, X., *Nature communications* **2016,** *7*.
6. Zhi, J.; Reiser, O.; Huang, F., *ACS Applied Materials & Interfaces* **2016,** *8* (13), 8452-8459. DOI 10.1021/acsami.5b12779.
7. Xu, H.; Hu, X.; Yang, H.; Sun, Y.; Hu, C.; Huang, Y., *Advanced Energy Materials* **2015,** *5* (6).
8. Wang, H.-g.; Ma, D.-l.; Huang, Y.; Zhang, X.-b., *Chemistry – A European Journal* **2012,** *18* (29), 8987-8993. DOI 10.1002/chem.201200434.
9. Chen, M.; Liu, J.; Chao, D.; Wang, J.; Yin, J.; Lin, J.; Jin Fan, H.; Xiang Shen, Z., *Nano Energy* **2014,** *9*, 364-372. DOI http://dx.doi.org/10.1016/j.nanoen.2014.08.011.
10. Wang, Y.; Zhou, T.; Jiang, K.; Da, P.; Peng, Z.; Tang, J.; Kong, B.; Cai, W.-B.; Yang, Z.; Zheng, G., *Advanced Energy Materials* **2014,** *4* (16), 1400696-n/a. DOI 10.1002/aenm.201400696.
11. Yadav, A. A.; Chavan, U. J., *Electrochimica Acta* **2017**.
12. Yu, Z.; Cheng, Z.; Wang, X.; Dou, S. X.; Kong, X., *Journal of Materials Chemistry A* **2017**.
13. Zuo, Y.; Ni, J. J.; Song, J. M.; Niu, H. L.; Mao, C. J.; Zhang, S. Y.; Shen, Y. H., *Applied Surface Science* **2016,** *370*, 528-535.
14. Zhu, L.; Peh, C. K. N.; Zhu, T.; Lim, Y. F.; Ho, G. W. W., *Journal of Materials Chemistry A* **2017,** *5*.
15. Cai, D.; Wang, D.; Liu, B.; Wang, L.; Liu, Y.; Li, H.; Wang, Y.; Li, Q.; Wang, T., *ACS applied materials & interfaces* **2014,** *6* (7), 5050-5055.
16. Zhou, W.; Cao, X.; Zeng, Z.; Shi, W.; Zhu, Y.; Yan, Q.; Liu, H.; Wang, J.; Zhang, H., *Energy & Environmental Science* **2013,** *6* (7), 2216-2221. DOI 10.1039/C3EE40155C.
17. Arico, A. S.; Bruce, P.; Scrosati, B.; Tarascon, J.-M.; Van Schalkwijk, W., *Nature materials* **2005,** *4* (5), 366-377.
18. Poizot, P.; Laruelle, S.; Grugeon, S.; Dupont, L.; Tarascon, J. M., *Nature* **2000,** *407* (6803), 496-499. DOI http://www.nature.com/nature/journal/v407/n6803/suppinfo/407496a0_S1.html.
19. Cui, C.; Xu, J.; Wang, L.; Guo, D.; Mao, M.; Ma, J.; Wang, T., *ACS Applied Materials & Interfaces* **2016,** *8* (13), 8568-8575. DOI 10.1021/acsami.6b02962.
20. Ramamoorthy, C.; Rajendran, V., *International Journal of Hydrogen Energy* **2017,** *42* (42), 26454-26463. DOI https://doi.org/10.1016/j.ijhydene.2017.07.078.
21. Ding, Z.; An, C.; Li, Q.; Hou, Z.; Wang, J.; Qi, H.; Qi, F., *Journal of Nanomaterials* **2010,** *2010* (1), 139-143.
22. Kalska-Szostko, B., *Electrochemical Methods in Nanomaterials Preparation*. InTech: **2012**.

23. Yan, J.; Fan, Z.; Wei, T.; Cheng, J.; Shao, B.; Wang, K.; Song, L.; Zhang, M., *Journal of Power Sources* **2009,** *194* (2), 1202-1207.

24. Kovalenko, V. L.; Kotok, V. A.; Sykchin, A. A.; Mudryi, I. A.; Ananchenko, B. A.; Burkov, A. A.; Sololvov, V. A.; Deabate, S.; Mehdi, A.; Bantignies, J. L., *Journal of Solid State Electrochemistry* **2016**, 1-9.

25. Hosono, E.; Wang, Y.; Kida, N.; Enomoto, M.; Kojima, N.; Okubo, M.; Matsuda, H.; Saito, Y.; Kudo, T.; Honma, I., *Acs Appl Mater Interfaces* **2010,** *2* (1), 212-218.

26. Li, M.; Xu, S.; Cherry, C.; Zhu, Y.; Wu, D.; Zhang, C.; Zhang, X.; Huang, R.; Qi, R.; Wang, L., *Journal of Materials Chemistry A* **2015,** *3* (26), 13776-13785.

27. Choudhary, N.; Chao, L.; Moore, J.; Nagaiah, N.; Lei, Z.; Jung, Y.; Thomas, J., *Advanced Materials* **2017,** *29* (21).

28. Furukawa, S.; Mehregany, M., *Sensors and Actuators A: Physical* **1996,** *56* (3), 261-266.

29. Peng, S.; Li, L.; Wu, H. B.; Madhavi, S.; Lou, X. W., *Advanced Energy Materials* **2015,** *5* (2), 1401172-n/a. DOI 10.1002/aenm.201401172.

30. Li, M.; Xu, S.; Cherry, C.; Zhu, Y.; Huang, R.; Qi, R.; Yang, P.; Wang, L.; Chu, P. K., *Electrochimica Acta* **2014,** *149*, 18-27.

31. Wang, T.; Pan, J.; Achille, K. G.; Sun, Y., *International Journal of Hydrogen Energy* **2017**.

32. Tong, X.; Wu, D.; Zhang, C.; Lian, K.; Xiong, D.; Xu, S.; Zhu, Y.; Qi, R.; Huang, R.; Wang, L., *Journal of Materials Chemistry A* **2016**.

33. Li, M.; Wang, Y.; Yang, H.; Chu, P. K., *Journal of Materials Chemistry A* **2017,** *5* (33), 17312-17324. DOI 10.1039/C7TA04981A.

34. Barmi, M. J.; Minakshi, M., *ChemPlusChem* **2016,** *81* (9), 964-977. DOI 10.1002/cplu.201600294.

35. Atuchin, V. V.; Khyzhun, O. Y.; Chimitova, O. D.; Molokeev, M. S.; Gavrilova, T. A.; Bazarov, B. G.; Bazarova, J. G., *Journal of Physics and Chemistry of Solids* **2015,** *77* (Supplement C), 101-108. DOI https://doi.org/10.1016/j.jpcs.2014.09.012.

36. Aguilera, L.; Leyet, Y.; Peña-Garcia, R.; Padrón-Hernández, E.; Passos, R. R.; Pocrifka, L. A., *Chemical Physics Letters* **2017,** *677* (Supplement C), 75-79. DOI https://doi.org/10.1016/j.cplett.2017.03.084.

37. Eda, K.; Uno, Y.; Nagai, N.; Sotani, N.; Stanley Whittingham, M., *Journal of Solid State Chemistry* **2005,** *178* (9), 2791-2797. DOI https://doi.org/10.1016/j.jssc.2005.06.014.

38. Rosić, M.; Zarubica, A.; Šaponjić, A.; Babić, B.; Zagorac, J.; Jordanov, D.; Matović, B., *Materials Research Bulletin* **2018,** *98* (Supplement C), 111-120. DOI https://doi.org/10.1016/j.materresbull.2017.10.015.

39. Hall, D. S.; Lockwood, D. J.; Bock, C.; Macdougall, B. R., *Proceedings Mathematical Physical & Engineering Sciences* **2015,** *471* (2174), 20140792.

40. Zhu, L.; Peh, C. K. N.; Zhu, T.; Lim, Y. F.; Ho, G. W. W., *Journal of Materials Chemistry A* **2017,** *5* (18), 8343-8351.

41. Yang, J.; Yu, C.; Fan, X.; Liang, S.; Li, S.; Huang, H.; Ling, Z.; Hao, C.; Qiu, J., *Energy & Environmental Science* **2016,** *9* (4), 1299-1307.

42. Zhang, X.; Xiao, J.; Zhang, X.; Meng, Y.; Xiao, D., *Electrochimica Acta* **2016,** *191* (12), 758-766.

43. Barral, G.; Njanjo-Eyoke, F.; Maximovitch, S., *Electrochimica Acta* **1995,** *40* (17), 2815-2828.

44. Brug, G.; Van Den Eeden, A.; Sluyters-Rehbach, M.; Sluyters, J., *Journal of electroanalytical chemistry and interfacial electrochemistry* **1984,** *176* (1), 275-295.

45. Gassa, L.; Vilche, J.; Ebert, M.; Jüttner, K.; Lorenz, W., *Journal of Applied Electrochemistry* **1990,** *20* (4), 677-685.

46. Orazem, M. E.; Tribollet, B., *Electrochemical impedance spectroscopy*. John Wiley & Sons: **2011**; Vol. 48.

47. Conway, B. E., *Electrochemical Supercapacitors: Scientific Fundamentals and Technological Applications*. Springer: **1999**.

48. Li, M.; Xu, S.; Cherry, C.; Zhu, Y.; Huang, R.; Qi, R.; Yang, P.; Wang, L.; Chu, P. K., *Electrochimica Acta* **2014,** *149*, 18-27. DOI http://dx.doi.org/10.1016/j.electacta.2014.10.091.

49. Zhang, X.; Xiao, J.; Zhang, X.; Meng, Y.; Xiao, D., *Electrochimica Acta* **2016,** *191* (Supplement C), 758-766. DOI https://doi.org/10.1016/j.electacta.2016.01.159.

50. Ke, Q.; Guan, C.; Zhang, X.; Zheng, M.; Zhang, Y.-W.; Cai, Y.; Zhang, H.; Wang, J., *Advanced Materials* **2017,** *29* (5), 1604164-n/a. DOI 10.1002/adma.201604164.

51. Zhang, Y.; Zhao, Y.; An, W.; Xing, L.; Gao, Y.; Liu, J., *Journal of Materials Chemistry A* **2017,** *5* (20), 10039-10047. DOI 10.1039/C7TA00963A.

52. Chen, Y.; Pang, W. K.; Bai, H.; Zhou, T.; Liu, Y.; Li, S.; Guo, Z., *Nano Letters* **2017,** *17* (1), 429-436. DOI 10.1021/acs.nanolett.6b04427.

53. Meng, X.; Deng, D., *Journal of Materials Chemistry A* **2016,** *4* (18), 6919-6925. DOI 10.1039/C5TA09329E.

54. Liu, S.; Lee, S. C.; Patil, U.; Shackery, I.; Kang, S.; Zhang, K.; Park, J. H.; Chung, K. Y.; Chan Jun, S., *Journal of Materials Chemistry A* **2017,** *5* (3), 1043-1049. DOI 10.1039/C6TA07842G.

55. Zhao, Y.; Hu, L.; Zhao, S.; Wu, L., *Advanced Functional Materials* **2016,** *26* (23), 4085-4093.

56. Dong, B.; Li, M.; Chen, S.; Ding, D.; Wei, W.; Gao, G.; Ding, S., *Acs Applied Materials & Interfaces* **2017,** *9* (21).

57. Li, M.; Xu, S.; Cherry, C.; Zhu, Y.; Wu, D.; Zhang, C.; Zhang, X.; Huang, R.; Qi, R.; Wang, L., *Journal of Materials Chemistry A* **2015,** *3* (26), 13776-13785.

58. Wang, F.; Zhu, S.; Li, M.; Lou, X.; Hui, K.; Xu, S.; Yang, P.; Wang, L.; Chen, Y.; Chu, P. K., *Journal of Alloys and Compounds* **2013,** *563*, 186-191.

59. Shen, J.; Li, X.; Wan, L.; Liang, K.; Tay, B. K.; Kong, L.; Yan, X., *ACS Applied Materials & Interfaces* **2017,** *9* (1), 668-676. DOI 10.1021/acsami.6b12370.

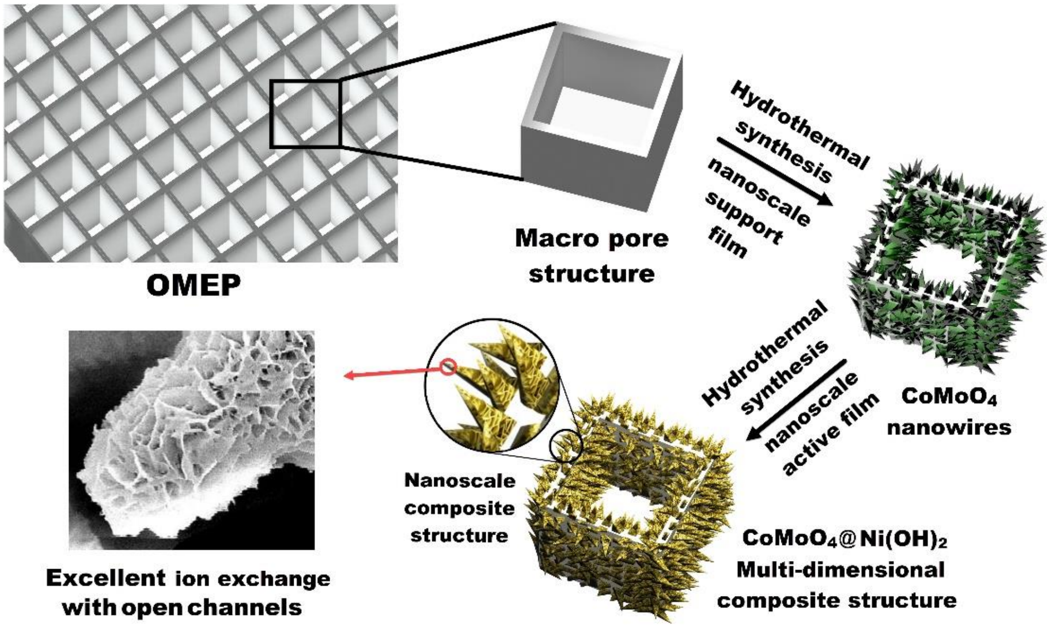

Fig.1 Illustration of the procedures to prepare the core-shell $CoMoO_4$@$Ni(OH)_2$/OMPE nanocomposite

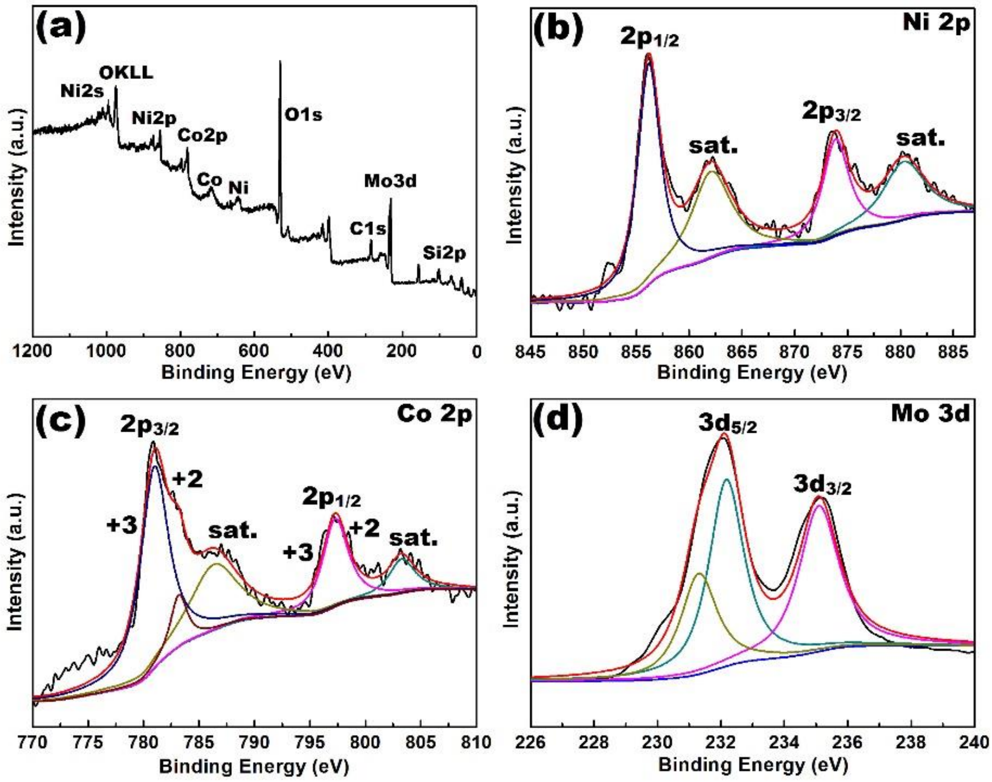

Fig.2 (a) XPS survey spectrum of $CoMoO_4$@$Ni(OH)_2$/OMEP; XPS spectra of (b) Ni 2p, (c) Co 2p, and (d) Mo 3d for $CoMoO_4$@$Ni(OH)_2$/OMEP.

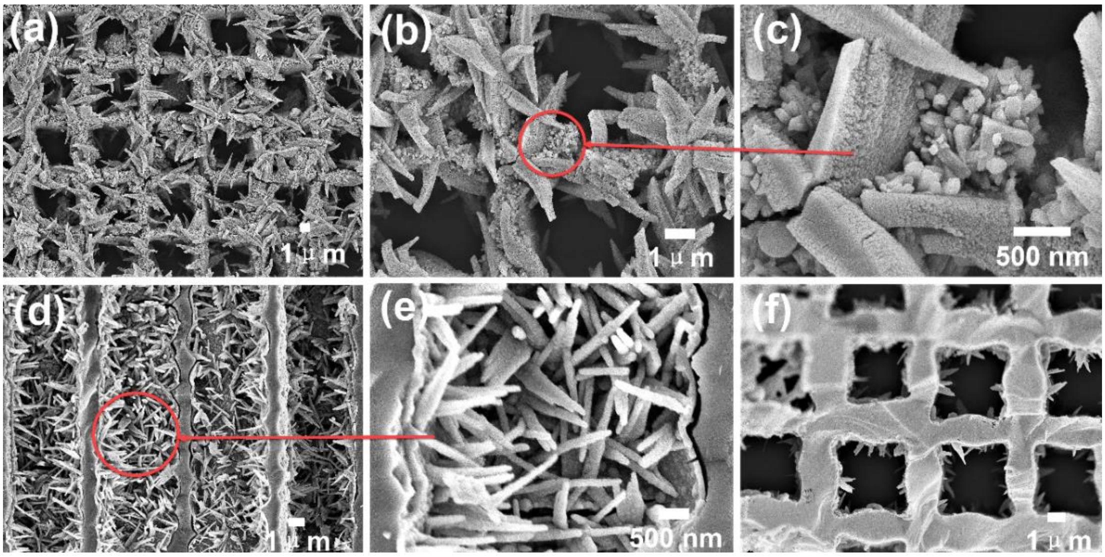

Fig.3 SEM images (a)–(c) of the $CoMoO_4$ on the surface of OMEP at different magnification; (d)-(e) the $CoMoO_4$ on the sidewall of OMEP at different magnification; (f) Observation of internal structure from cross section of $CoMoO_4$/OMEP.

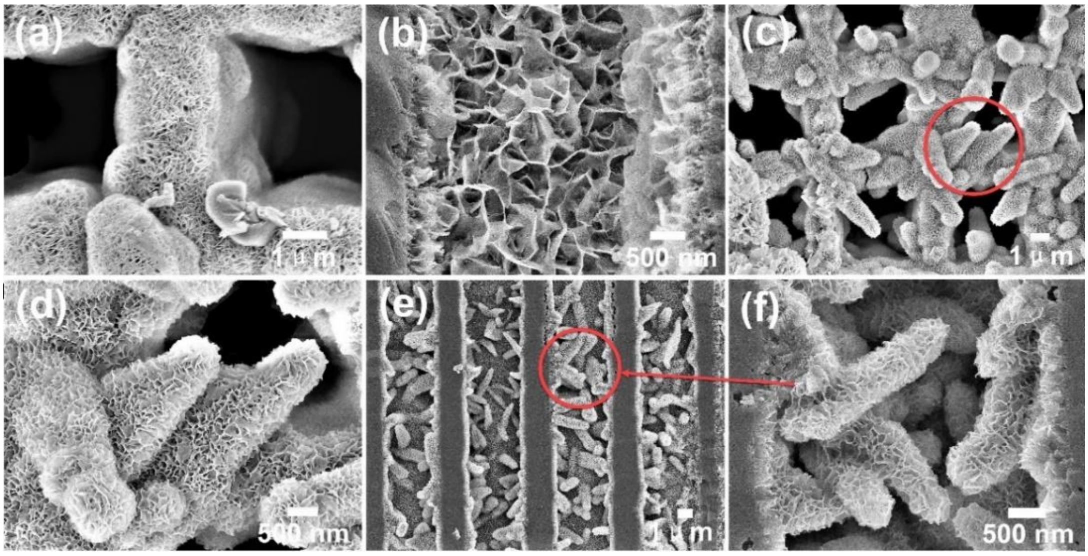

Fig. 4 SEM images of the $Ni(OH)_2$ on the surface (a) and on the side wall (b) of OMEP; SEM images of the core-shell $CoMoO_4@Ni(OH)_2$ nanocomposite on the surface (c)–(d) and on the inter sidewall (e)-(f) of OMEP at different magnification.

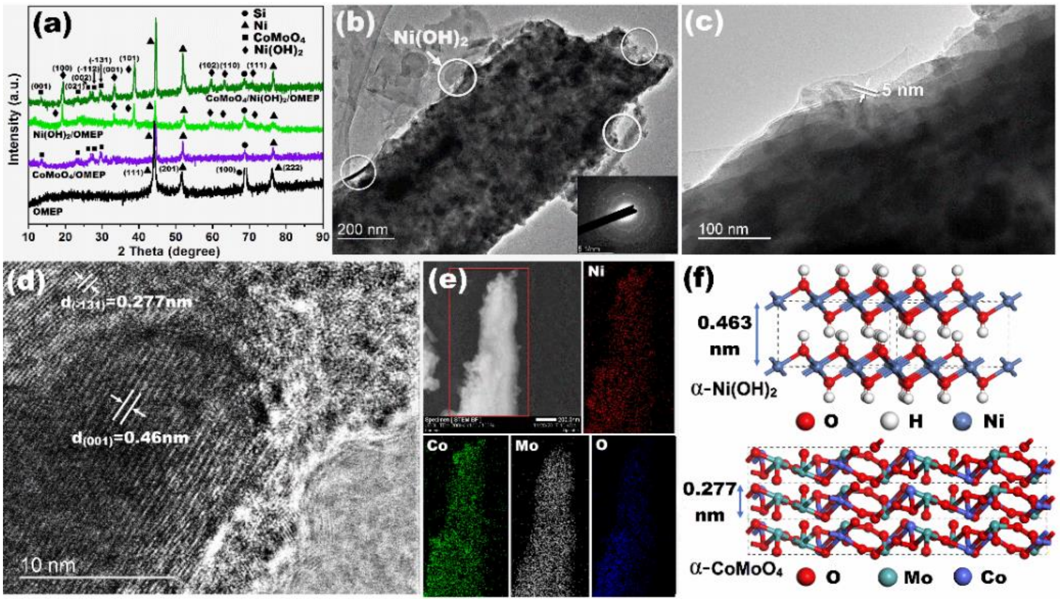

Fig.5 (a) XRD pattern of OMEP, $CoMoO_4$/OMEP, $Ni(OH)_2$/OMEP and $CoMoO_4$@$Ni(OH)_2$/OMEP; (b)-(c) TEM images and SAED patterns of $CoMoO_4$@$Ni(OH)_2$ core–shell composite nanostructure; (d) magnified view of HR-TEM image of $CoMoO_4$@$Ni(OH)_2$; (e) EDS maps of $Ni(OH)_2$; (f) lattice structure of $Ni(OH)_2$ and $CoMoO_4$.

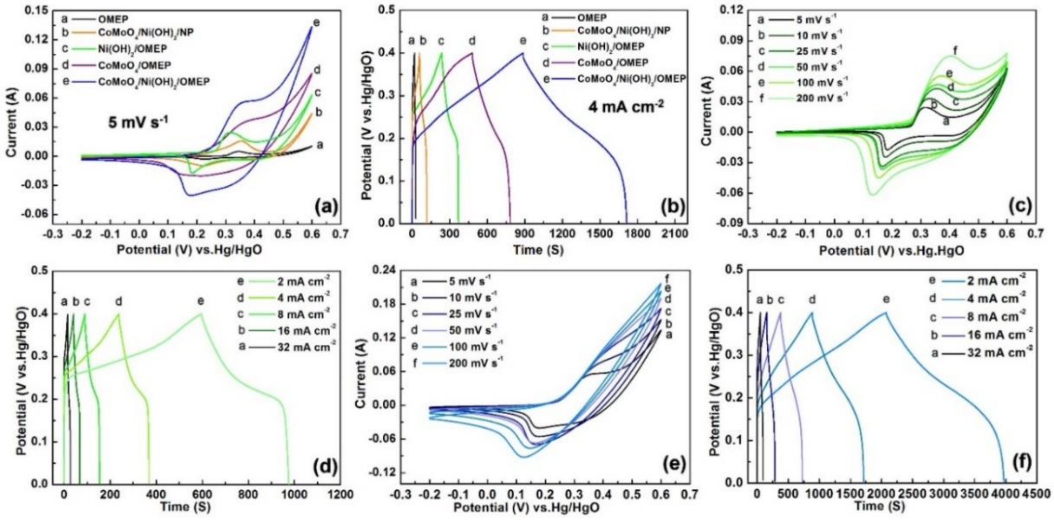

Fig.6 (a) Cyclic voltammetry curves at the scanning rate of 5 mV S−1 and (b) CP curves at 4 mA cm−2of the activated fabricated OMEP, $CoMoO_4$@$Ni(OH)_2$/NP, $CoMoO_4$/OMEP, $Ni(OH)_2$/OMEP, $CoMoO_4$@$Ni(OH)_2$/OMEP and electrode; (c) and (e) CV curves of $Ni(OH)_2$/OMEP and $CoMoO_4$@$Ni(OH)_2$/OMEP at different scanning rates; (d) and (f) CP curves of $Ni(OH)_2$/OMEP and $CoMoO_4$@$Ni(OH)_2$/OMEP at different current densities after activation.

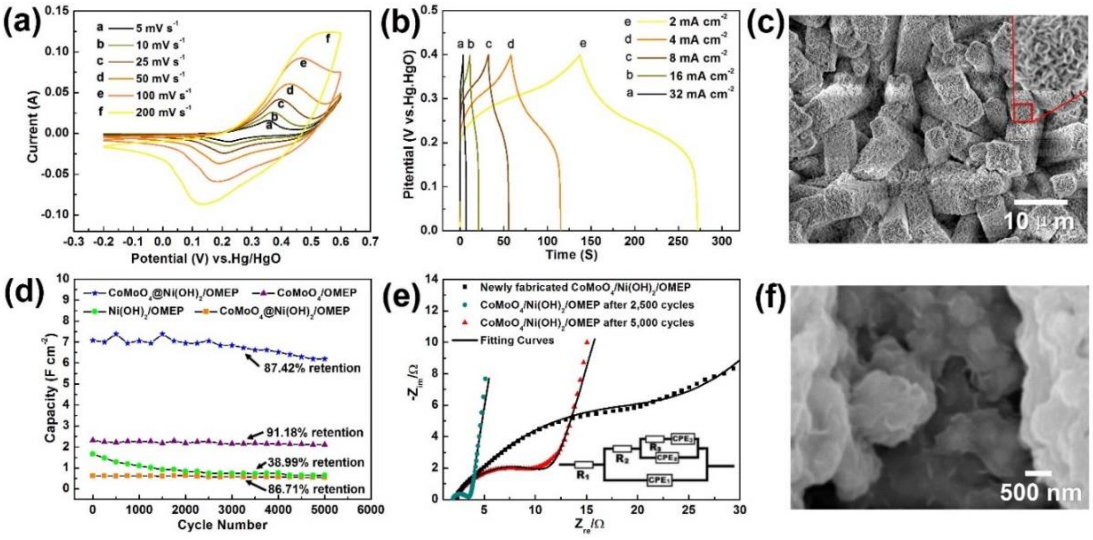

Fig. 7 (a) the CV curves and CP curves of $CoMoO_4@Ni(OH)_2$/NP; (c) SEM image of the surface of $CoMoO_4@Ni(OH)_2$/NP electrode; (d) Long-term performance of the electrodes assessed at a charging–discharging current density of 100 mA cm^{-2}; (e) Nyquist plots of the newly fabricated $CoMoO_4@Ni(OH)_2$/OMEP electrode and that after 2,500 cycles and after 5,000 cycles of the long-term performance test with the equivalent circuit; (f) morphological characteristics of $CoMoO_4@Ni(OH)_2$ composite on the sidewall of OMEP after 5,000 cycles.

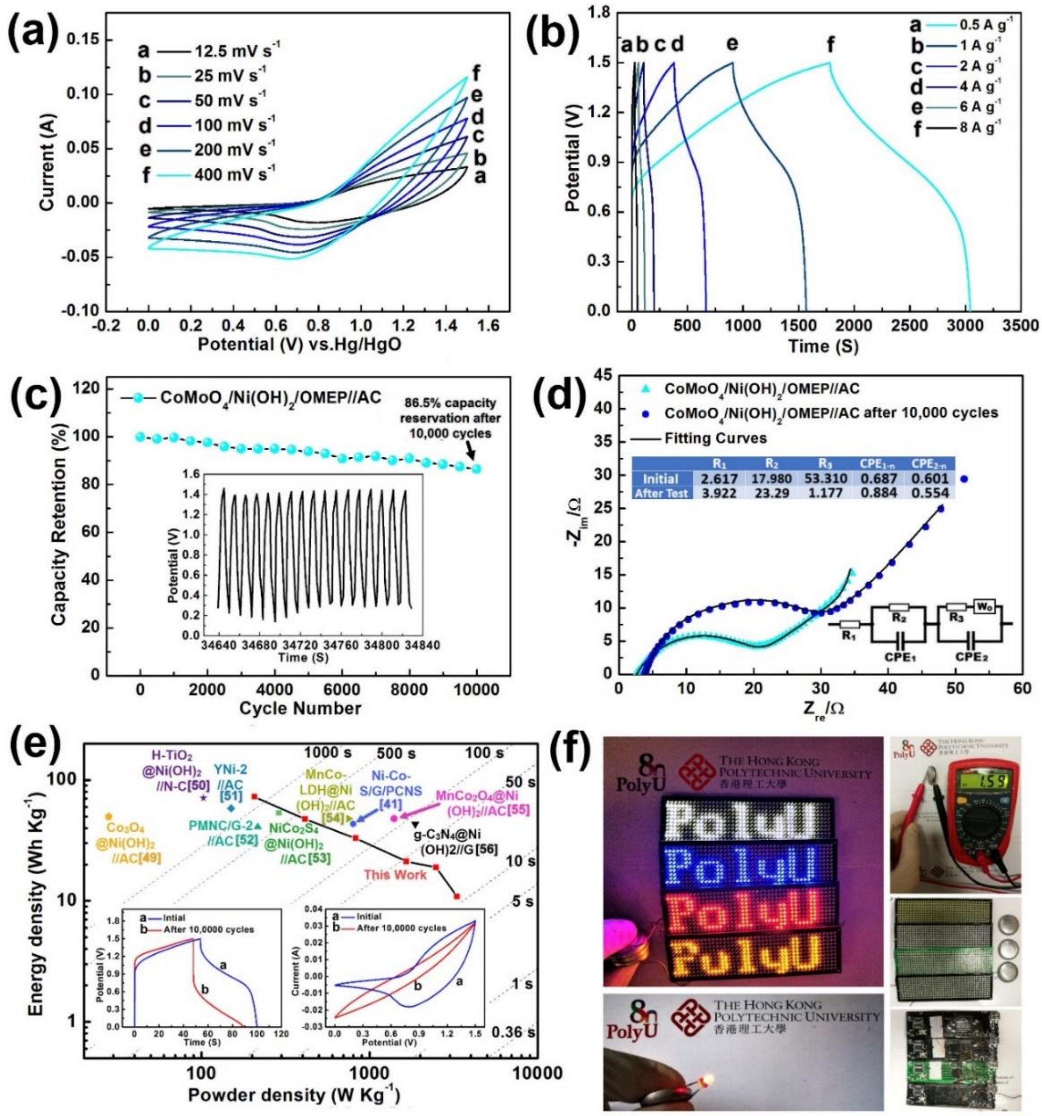

Fig. 8 (a) CVs acquired at different scanning rates and (b) CP curves at different current densities between 0 and 1.5 V of the ASC; (c) cycling stability of the 10,000 cycles of device at large current densities and cycle curve in the intermediate stage; (d) Nyquist plots of the as-assembled ASC before and after 10,000 cycles in the long-term performance test with the equivalent circuit and elements fitting the impedance curve; (e) Ragone plot of the as-assembled ASC (insets is the comparison of CV and IT curves from the as-assembled ASC before and after 10,000 cycles); (f) four parallel programmed LED arrays powered by the three parallel as-assembled ASCs, more than 1.59 V voltage window of the one ASC can power a red 5mm LED, the as-assembled ASCs, and positive and negative sides of the LED arrays.

Support information:

Core-shell $CoMoO_4/Ni(OH)_2$ on Ordered Micro-Porous Electrode Plate as the composite structure electrode for high performance supercapacitor

Mai Li[a*], Yuanhao Wang[b], Lianwei Wang[c], Hongxing Yang[a*] and Paul K Chu[d]

a Renewable Energy Research Group, Department of Building Services Engineering, The Hong Kong Polytechnic University, Hung Hom, Kowloon, Hong Kong, China
b Faculty of Science and Technology, Technological and Higher Education Institute of Hong Kong, New Territories, Hong Kong, China
c Key Laboratory of Polar Materials and Devices, Ministry of Education, Department of Electronic Engineering, East China Normal University, 500 Dongchuan Road, Shanghai 200241, P. R. China
d Department of Physics and Material Science, City University of Hong Kong, Tat Chee Avenue, Kowloon, Hong Kong, China
* Corresponding author: Tel.: +852 56065568; Fax: +852 2766 7198.
E-mail address: mai.li@polyu.edu.hk.

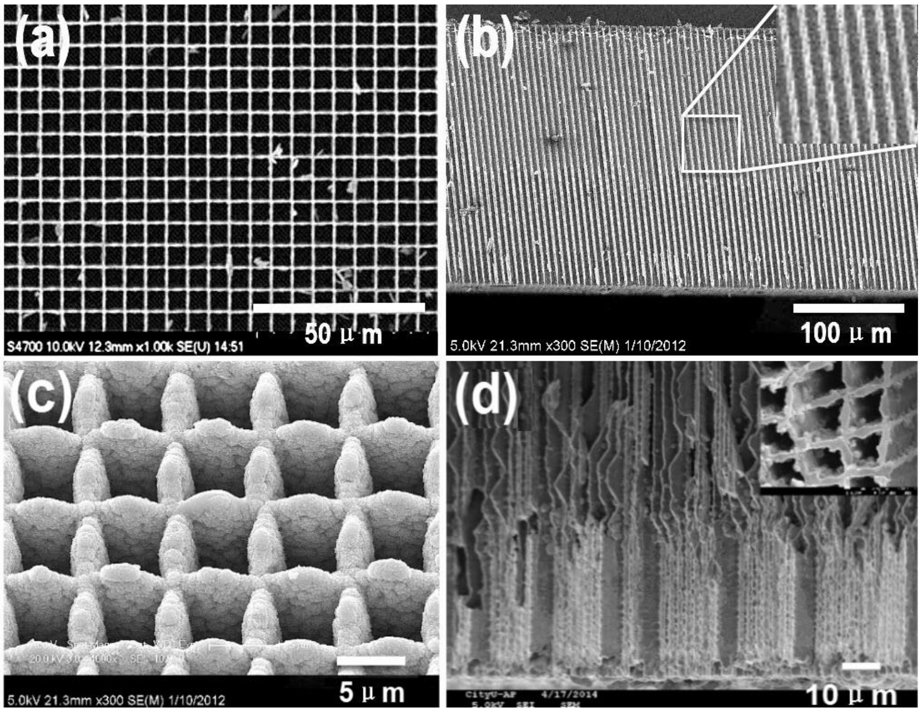

Fig.S1 FE-SEM images acquired from (a) the ordered Si-MCP; (b) cross-sectional view of ordered Si-MCP; (c) surface of nano-Ni covered OMEP; and (d) cross-sectional view of the nano-Ni covered OMEP

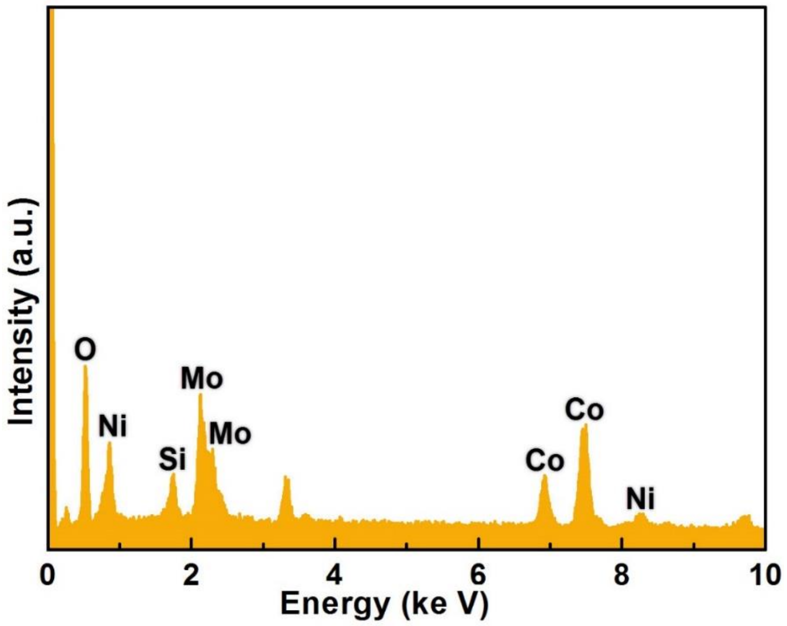

Fig.S2 The EDS of the $CoMoO_4$@$Ni(OH)_2$/OMEP electrode.

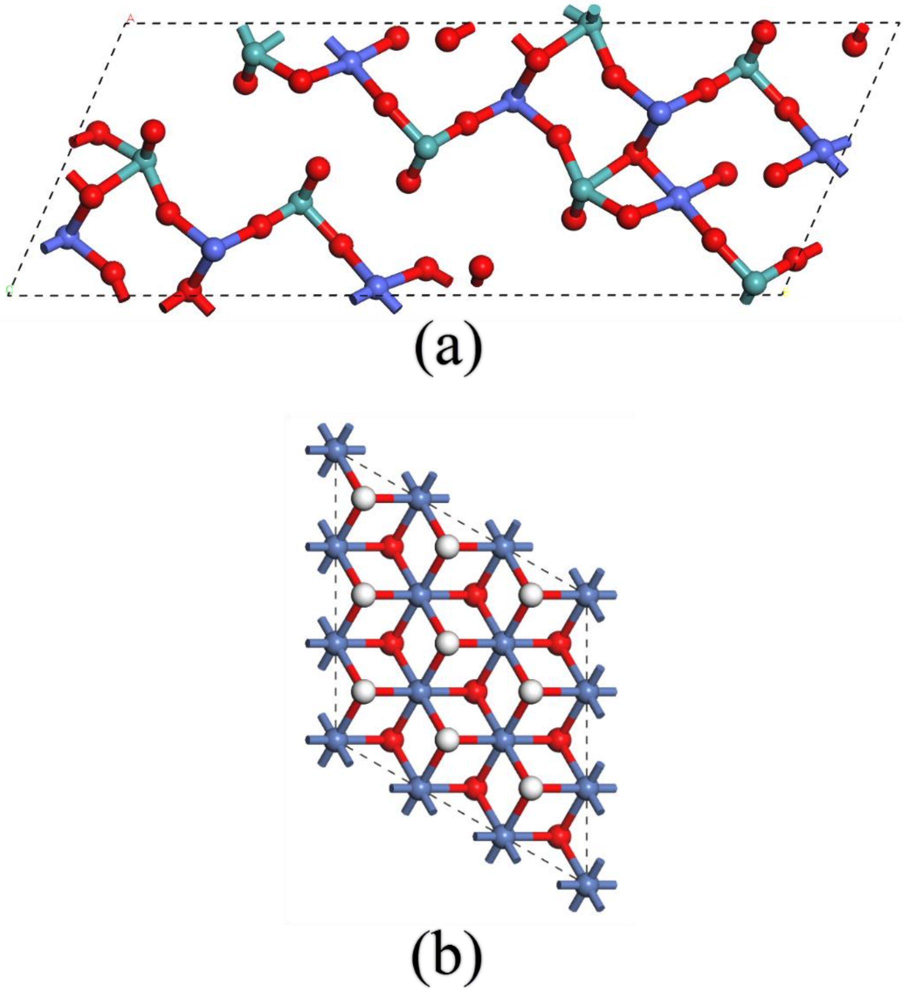

Fig.S3 (a) (-131) plane of α-$CoMoO_4$; (b) (001) planeof α-$Ni(OH)_2$

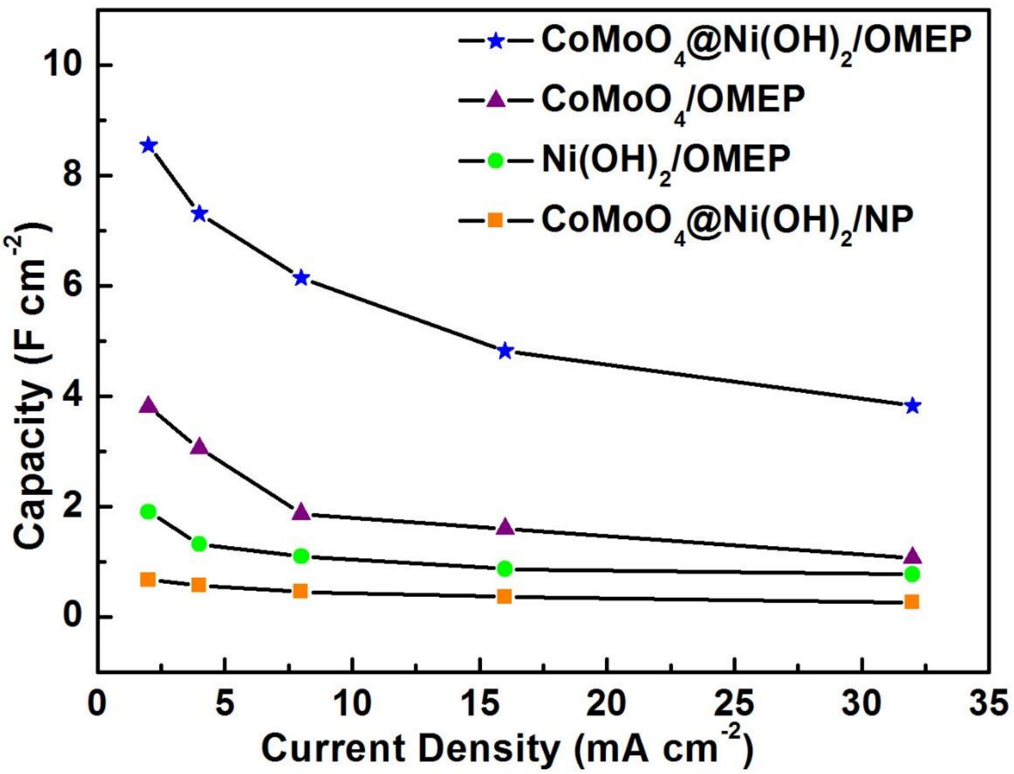

Fig.S4 Variation of the interfacial capacitance of the $CoMoO_4$@$Ni(OH)_2$/OMEP, $CoMoO_4$/OMEP, $Ni(OH)_2$/OMEP, $CoMoO_4$@$Ni(OH)_2$/NP with different current densities.

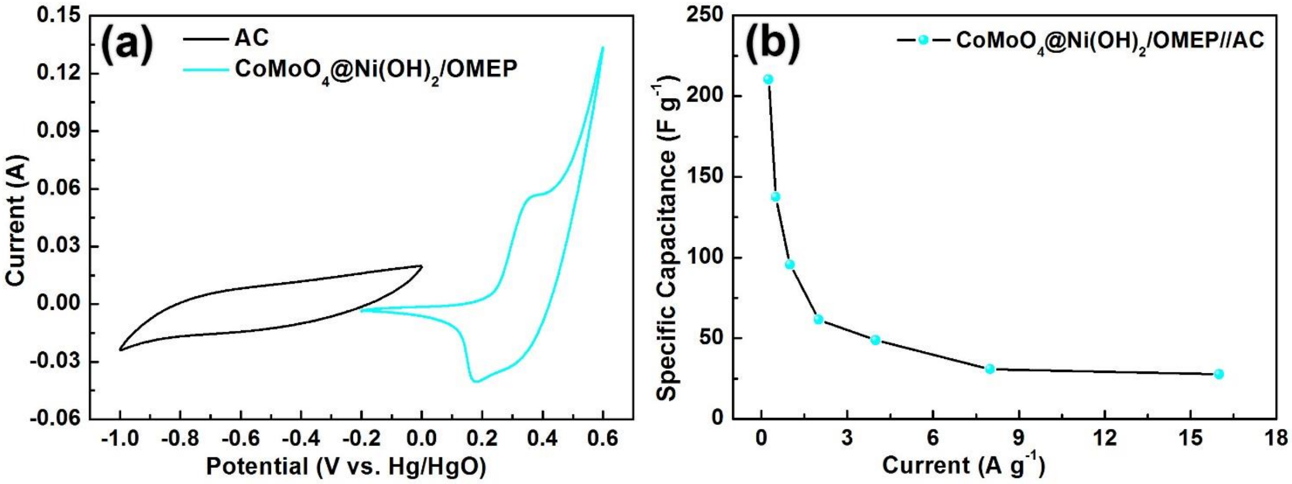

Fig. S5 (a) CV curves comparison between $CoMoO_4$@$Ni(OH)_2$/OMEP (0 to 0.4V) and AC (-1 to 0V) at a scanning rate of 30 mV s^{-1}; (b) Specific capacitance values of the $CoMoO_4$/$Ni(OH)_2$/OMEP//AC asymmetrical supercapacitor with the change of charge-discharge current density form 0.25 A g^{-1} to 16 A g^{-1}.

	R_1(Ω)	R_2(Ω)	R_3(Ω)	CPE_1	CPE_2	CPE_3
Initial	2.34	5.65	26.32	1.35	0.47	0.46
After 2,500 cycles	1.99	1.27	1.73	1.39	1.46	0.87
After 5,000 cycles	2.11	2.84	10.95	1.24	1.24	0.76

Table 1 The EIS fitting indexes of the CoMoO4/Ni(OH)2/OMEP from its long time cycling test of initial, after 2500 cycles and after 5000 cycles.

Table 2. Comparison of the as-assembled ASCs with those reported in the literature.

Electrode composition	**Electrolyte**	**Specific Capacitance (F cm^{-2} or F g^{-1})**	**Voltage HI Limit (V)**	**Maximum energy density (W h kg^{-1})**	**Maximum power density (W kg^{-1})**	**Full cell Cyclic ability (retention)**	**Ref.**
PMNC/G-2//AC	KOH solution	or 1762	1.4	41	216	83% after 10,000 cycles	[1]
Co_3O_4@$Ni(OH)_2$//AC	KOH solution	or 912	1.6	49.8	28.1	95% after 2,000 cycles	[2]
H-TiO_2@$Ni(OH)_2$//N-C	KOH solution	or 303	1.8	70.9	102.9	90% after 5,000 cycles	[3]
MnCo-LDH@$Ni(OH)_2$//AC	KOH solution	or 2320	1.5	47.9	750.7	90.9% after 5,000 cycles	[4]
YNi-2//AC	KOH solution	or 1860	1.5	58.4	150.048		[5]
g-C3N4@Ni(OH)2//Graphene	KOH solution	or 1768.7	1.3	43.1	19.3	72% after 8,000 cycles	[6]
Ni–Co–S/G//PCNS	KOH solution	or 1492	1.6	43.3	800	85% after 10,000 cycles	[7]
NiCo2S4@Ni(OH)2//AC	KOH solution		1.7	53.3	290	98.8% after 2,000 cycles	[8]
Ni–Co–S/G//PCNS	KOH solution	8.55 or 1858.70	1.5	65.73	187.5	86.5% after 10,000 cycles	This Work

Reference

[1] Y. Chen, W.K. Pang, H. Bai, T. Zhou, Y. Liu, S. Li, Z. Guo, Enhanced Structural Stability of Nickel–Cobalt Hydroxide via Intrinsic Pillar Effect of Metaborate for High-Power and Long-Life Supercapacitor Electrodes, Nano Letters, 17 (2017) 429-436.

[2] X. Zhang, J. Xiao, X. Zhang, Y. Meng, D. Xiao, Three-Dimensional Co3O4 Nanowires@Amorphous Ni(OH)2 Ultrathin Nanosheets Hierarchical Structure for Electrochemical Energy Storage, Electrochimica Acta, 191 (2016) 758-766.

[3] Q. Ke, C. Guan, X. Zhang, M. Zheng, Y.-W. Zhang, Y. Cai, H. Zhang, J. Wang, Surface-Charge-Mediated Formation of H-TiO2@Ni(OH)2 Heterostructures for High-Performance Supercapacitors, Advanced Materials, 29 (2017) 1604164-n/a.

[4] S. Liu, S.C. Lee, U. Patil, I. Shackery, S. Kang, K. Zhang, J.H. Park, K.Y. Chung, S. Chan Jun, Hierarchical MnCo-layered double hydroxides@Ni(OH)2 core-shell heterostructures as advanced electrodes for supercapacitors, Journal of Materials Chemistry A, 5 (2017) 1043-1049.

[5] Y. Zhang, Y. Zhao, W. An, L. Xing, Y. Gao, J. Liu, Heteroelement Y-doped [small alpha]-Ni(OH)2 nanosheets with excellent pseudocapacitive performance, Journal of Materials Chemistry A, 5 (2017) 10039-10047.

[6] B. Dong, M. Li, S. Chen, D. Ding, W. Wei, G. Gao, S. Ding, Formation of g-C3N4@Ni(OH)2 honeycomb nanostructure and asymmetric supercapacitor with high energy and power density, Acs Applied Materials & Interfaces, 9 (2017).

[7] J. Yang, C. Yu, X. Fan, S. Liang, S. Li, H. Huang, Z. Ling, C. Hao, J. Qiu, Electroactive edge site-enriched nickel–cobalt sulfide into graphene frameworks for high-performance asymmetric supercapacitors, Energy & Environmental Science, 9 (2016) 1299-1307.

[8] X. Meng, D. Deng, Bio-inspired synthesis of [small alpha]-Ni(OH)2 nanobristles on various substrates and their applications, Journal of Materials Chemistry A, 4 (2016) 6919-6925.